

Universal Entanglement Revival of Topological Origin

Dongni Chen

Department of Physics, Korea University, Seoul 02841, South Korea

Stefano Chesi

Beijing Computational Science Research Center, Beijing 100193, People's Republic of China

Department of Physics, Beijing Normal University, Beijing 100875, People's Republic of China

Mahn-Soo Choi

Department of Physics, Korea University, Seoul 02841, South Korea

E-mail: choims@korea.ac.kr

Abstract. We have analyzed the dynamics of entanglement in dissipative fermionic and bosonic Su–Schrieffer–Heeger (SSH) models and found that, when the decoherence channel preserves the chiral symmetry, they exhibit a revival of entanglement in a wide range of parameters. This behavior only emerges in the topological phase, with the visibility of the revival dropping to zero at the phase boundary. Furthermore, the revival acquires a universal character once the system size exceeds the localization length of the edge modes. Our findings indicate that the universal entanglement revival has its origin in the topological properties of the SSH model. These dynamical properties may be experimentally accessible, for example, using photonic quantum computers.

1. Introduction

Entanglement is a critical resource in quantum information processing, yet is intrinsically fragile with respect to interactions with the environment. These induce decoherence, which typically leads to the rapid degradation of entanglement. Nevertheless, certain systems have been shown to exhibit the interesting phenomenon of entanglement revival, in which, after the initial decay, an unexpected recovery occurs at a later stage of the dynamical evolution [1–16]. A robust mechanism causing this type of dynamics has been recently discussed for an ensemble of three-level systems interacting with single-mode bosons [16], where the revival is associated to the presence of a special zero-energy state weakly affected by decoherence. The dissipative evolution rapidly destroys the initial

entanglement but eventually turns itself into a self-purification process, resulting in a distinct entanglement revival.

The mechanism of Ref. [16] is generic, thus might be applicable to other scenarios. Indeed, we show here that topological system are a natural candidate to observe this type of revivals. The potential relevance of Ref. [16] for topological systems is suggested by the crucial role played in the three-level ensemble by a chiral symmetry, and by the fact that the state responsible for the revival belongs to the zero-energy subspace associated with that symmetry. In this sense, the metastable state of Ref. [16] is analogous to the zero-energy edge mode of a topological system.

To explore concretely these ideas, we specialize our analysis to a dissipative version of the Su-Schrieffer-Heeger (SSH) model. The SSH model is a well-known paradigm for topological insulators [17–19] and has considerable relevance for quantum information and quantum computing applications [20–25], due to its robustness against disorder and defects [26–32]. Recent studies have increasingly focused on how topological systems, including the SSH model, behave under dissipative dynamics [33–38]. Gaining a deeper understanding of dissipation in topologically protected systems is critical for furthering the practical implementation of quantum technologies. Here we explore how the topological properties of the SSH model influence entanglement dynamics, which is of significant interest for the development of more resilient quantum systems.

The topological edge states of the SSH model remain stable when decoherence only acts on one of the two sublattices (specifically, the odd sites). Under this scenario, we find the occurrence of an entanglement revival directly tied to the presence of a topological edge mode. We also show that the revival approaches a universal form when increasing the system size, i.e., the evolution of entanglement becomes independent of the chain length. Therefore, the presence (absence) of the revival is a definite signature of the topological (trivial) phase. Our findings apply to both fermionic and bosonic versions of the SSH model, thus they could be simulated in a controlled manner using photonic quantum computers [39–41]. Nearest-neighbor hoppings of variable coupling strengths can be realized with tunable beam splitters. Additionally, the required photon loss pattern — lower at even sites and higher at odd sites — can be simulated by selective leakage of photons. Therefore, we expect that the topologically protected entanglement revivals discussed here are achievable with current photonic technology.

This paper is organized as follows: In Section 2, we introduce the SSH model, briefly reviewing its chiral symmetry and topological properties. The theoretical methods we used are detailed in Section 3, including the semiclassical approach and different entanglement measures. Section 4 presents the results, highlighting the universal entanglement revival observed in both fermionic and bosonic SSH models as well as its connection to topological edge states. Section 5 concludes the paper. To further support the arguments in the main text, two appendices are provided: [Appendix A](#) demonstrates the universal revival behavior in the mutual information as an alternative extent of entanglement. [Appendix B](#) examines the density of von Neumann and Rényi entropies, which also exhibit a universal behavior.

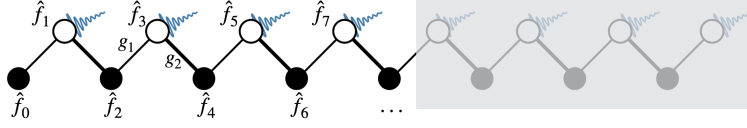


Figure 1. Schematics of the dissipative Su-Schrieffer-Heeger (SSH) model. The coupling strengths between nearest-neighbor sites alternate between two values, g_1 and g_2 , and the quantum decoherence process (wavy lines) occurs only at the odd sites. For numerical efficiency, we ignore the shaded region and denote the remaining part as ‘half-SSH chain’.

2. Model

The SSH model is a prototype of one-dimensional (1D) topological insulators [18,19]. As a tight-binding model with alternating hopping amplitudes, g_1 and g_2 , it exhibits a *chiral symmetry* (also known as *sub-lattice symmetry*), which, together with the time-reversal symmetry, completely classifies the topological states of matter. The chiral symmetry is characterized by a unitary operator that *anti-commutes* with the Hamiltonian, and ensures that the Hamiltonian matrix can be written in a block-off-diagonal form, leading to a degenerate zero-energy subspace and a symmetric energy spectrum around zero energy. The zero-energy states are especially interesting: According to the bulk-boundary correspondence principle, they always accompany the topologically non-trivial phase of topological insulators and are localized at the boundaries of the system. In the SSH model, the topological phase occurs when $g_1 < g_2$ ‡. In this phase, there are two zero-energy edge states at the two ends of the chain. The *localization length* of each edge state describes how far the state spreads from the edge into the bulk of the chain, and is given by $\xi = 2/\log[g_2/g_1] + 1$.

For systems of sufficiently large size $L \gg \xi$, the zero-energy edge states at the two ends are decoupled from each other. As the effects of interest in this work only involve a single edge state, we will, for the sake of numerical efficiency, consider only half of the physically realistic chain, ignoring the shaded portion in Fig. 1 §. This simplification allows us to concentrate on the properties and behavior of a single edge state, while maintaining the essential features of the topological phase. This half-SSH model contains n two-site unit cells and a single unpaired site, so the overall chain length $L = 2n + 1$ is always odd. The Hamiltonian reads:

$$\hat{H} = \sum_{i=1}^{(L-1)/2} \left(g_1 \hat{f}_{2i-2}^\dagger \hat{f}_{2i-1} + g_2 \hat{f}_{2i-1}^\dagger \hat{f}_{2i} \right) + \text{H.c.}, \quad (1)$$

where \hat{f}_i^\dagger and \hat{f}_i are, respectively, the creation and annihilation operators at site $i = 0, 1, \dots, L - 1$. In the fermionic (bosonic) SSH model, they satisfy the anti-

‡ Without loss of generality, we assume real and positive hopping amplitudes. Complex hopping amplitudes can always be brought to real positive values with a gauge transformation.

§ In this half-chain model one unit cell is not complete, as it contains only a single site instead of two. Therefore, the bulk-boundary correspondence does not hold in the usual sense.

commutation (commutation) relations, $\{\hat{f}_i, \hat{f}_j^\dagger\} = \delta_{ij}$ ($[\hat{f}_i, \hat{f}_j^\dagger] = \delta_{ij}$). To better reveal the consequences of the chiral symmetry and the topological properties of the system, we rewrite the Hamiltonian in terms of the normal modes $\hat{C}_{\pm k}$:

$$\hat{H} = \sum_{k=1}^{(L-1)/2} \epsilon_k \left(\hat{C}_k^\dagger \hat{C}_k - \hat{C}_{-k}^\dagger \hat{C}_{-k} \right), \quad (2)$$

where the single-particle energies $\pm\epsilon_k$ are given by:

$$\epsilon_k := \sqrt{g_1^2 + g_2^2 + 2g_1g_2 \cos(\tilde{k})}, \quad (3)$$

with $\tilde{k} := 2\pi k/(L+1)$. The normal modes are related to the site operators \hat{f}_i by

$$\hat{C}_{\pm k} = \sum_{i=0}^{(L-1)/2} A_{ki} \hat{f}_{2i} \pm \sum_{i=1}^{(L-1)/2} B_{ki} \hat{f}_{2i-1}, \quad (4)$$

with

$$A_{ki} := \sqrt{\frac{2}{L+1}} \sin(\tilde{k}i + \phi_k), \quad (5a)$$

$$B_{ki} := \sqrt{\frac{2}{L+1}} \sin(\tilde{k}i), \quad (5b)$$

and $\cos(\phi_k) := (g_1 \cos \tilde{k} + g_2)/\epsilon_k$. Furthermore, there is a special normal mode with zero energy, which does not appear in Eq. (2):

$$\hat{C}_0 = \sqrt{\frac{1 - (g_1/g_2)^2}{1 - (g_1/g_2)^{L+1}}} \sum_{i=0}^{(L-1)/2} (-g_1/g_2)^i \hat{f}_{2i}. \quad (6)$$

Clearly, when $g_1 < g_2$ this mode has its probability amplitudes localized at the left end of the system \parallel . For later use, when $k = 0$ we define:

$$A_{0i} = \sqrt{\frac{1 - (g_1/g_2)^2}{1 - (g_1/g_2)^{L+1}}} (-g_1/g_2)^i. \quad (7)$$

Recall that, unlike this zero-energy edge mode, all other modes $\hat{C}_{\pm k}$ ($k \neq 0$) are bulk states with probability amplitudes spread over the whole chain.

We are interested in the topological influence on the dynamics of quantum entanglement in the presence of decoherence. To clearly illustrate the topological effects, we assume that the quantum decoherence processes preserve the chiral symmetry; that is, we assume that decoherence processes occur only on the odd sites \hat{f}_{2i-1} , with a uniform decay rate Γ . The noisy dynamics is governed by the quantum master equation

$$\frac{d\hat{\rho}}{dt} = -i[\hat{H}, \hat{\rho}] + \Gamma \sum_{i=1}^{(L-1)/2} \mathcal{D}[\hat{f}_{2i-1}]\hat{\rho}, \quad (8)$$

\parallel In the full SSH model, there is another zero-energy edge mode at the right end.

where $\hat{\rho}$ is the density operator of the system and \mathcal{D} is the superoperator $\mathcal{D}[\hat{f}]\hat{\rho} = \hat{f}\hat{\rho}\hat{f}^\dagger - (\hat{f}^\dagger\hat{f}\hat{\rho} + \hat{\rho}\hat{f}^\dagger\hat{f})/2$, describing the quantum decoherence processes.

We will consider an initial state of the form:

$$|\psi_g\rangle = \hat{C}_0^\dagger \prod_{k=1}^{(L-1)/2} \hat{C}_{-k}^\dagger | \rangle, \quad (9)$$

where $| \rangle$ is the vacuum state. Since all negative-energy modes and the zero-energy mode are singly occupied, this initial state is one of the two degenerate many-body ground states of the fermionic model. In that case, it is a natural choice for the initial state. In the bosonic model, occupying all negative and zero-energy normal modes can be achieved by using external driving, as commonly done in experimental demonstrations of topological band structures, e.g., in photonic crystals [42, 43]. Since we study non-equilibrium dynamics, the resulting physical effects inevitably depend on the initial state. However, as long as the zero-energy edge mode is initially occupied, our main findings remain qualitatively valid for many other initial states. In particular, we have checked that a universal revival is found for an initial state where all the normal modes are singly occupied. This confirms that the universal entanglement dynamics reported below is closely related to topological features.

3. methods

Before presenting in Sec. 4 our main results, we describe in this Section the methods used to solve the quantum master equation, Eq. (8), and to analyze the entanglement content of the solution.

3.1. Semiclassical approach

The computational cost to exactly solve the quantum master equation increases exponentially with system size ¶. Fortunately, in the parameter regime of our interest, a semiclassical approach provides an accurate description of the dynamics. We first note that, when the coupling strengths are much larger than the decay rate ($g_1, g_2 \gg \Gamma$), the eigenstates of Eq. (1) are generally well-separated in energy. Since the coherent phase factor between two eigenstates oscillates rapidly in time, it gets averaged out throughout the slow dissipative evolution and we may assume that $\hat{\rho}(t)$ is approximately diagonal in the many-body eigenstates, $|E_\alpha\rangle$:

$$\hat{\rho}(t) \approx \sum_{\alpha} |E_\alpha\rangle P_\alpha(t) \langle E_\alpha|. \quad (10)$$

The probabilities P_α of different many-body eigenstates $|E_\alpha\rangle$ satisfy the master equation

$$\frac{dP_\alpha(t)}{dt} = \sum_{\beta} (\gamma_{\alpha\beta} P_\beta(t) - \gamma_{\beta\alpha} P_\alpha(t)), \quad (11)$$

¶ For non-interacting fermions with a restricted class of quantum jump operators, a polynomial-time method is available. See, for example, Refs. [44, 45].

where the transition rate $\gamma_{\alpha\beta}$ from $|E_\beta\rangle$ to $|E_\alpha\rangle$ is given by $\gamma_{\alpha\beta} := \Gamma \sum_{i=1}^{(L-1)/2} |\langle E_\alpha | \hat{f}_{2i-1} | E_\beta \rangle|^2$. In terms of the eigenmode operators:

$$\gamma_{\alpha\beta} := \frac{\Gamma}{2} \sum_{k \neq 0} |\langle E_\alpha | \hat{C}_k | E_\beta \rangle|^2, \quad (12)$$

which can be derived using $\sum_{i=1}^{(L-1)/2} B_{ki} B_{k'i} = \delta_{kk'}/2$. This relation has its origin in the chiral symmetry, leading to coefficients A_{ki} and B_{ki} , see Eqs. (5) and (7), which are *separately* normalized. Therefore, we also have $\sum_{i=0}^{(L-1)/2} A_{ki} A_{k'i} = \delta_{kk'}/2$.

We note some unique properties of the semiclassical dynamics described by Eqs. (10) and (11). First, every time a decay process occurs, the total number of particles decreases by one. However, the zero-energy edge state can never decay, because \hat{C}_0 has non-zero amplitudes only at the even sites, see Eq. (6). In the long-time limit ($t \rightarrow \infty$) only one particle remains, occupying the zero-energy edge state:

$$\hat{\rho}_\infty := \lim_{t \rightarrow \infty} \hat{\rho}(t) = \hat{C}_0^\dagger | \rangle \langle | \hat{C}_0. \quad (13)$$

Second, with the initial condition Eq. (9) the occupation numbers of the eigenmodes are either one or zero, and a decay process corresponds to one of the occupied modes becoming empty. From Eq. (12), we see that all these decays occur with an identical rate, $\Gamma/2$, which allows us to solve the semiclassical evolution of Eqs. (10) and (11) in closed form:

$$\hat{\rho}(t) \approx \sum_{m=0}^{(L-1)/2} P_{m+1}(t) \sum_{\{k_i\}_{i=1}^m} \hat{C}_{\{k_i\}}^\dagger \hat{\rho}_\infty \hat{C}_{\{k_i\}}, \quad (14)$$

with

$$P_{m+1}(t) = \exp \left[\frac{-m\Gamma t}{2} \right] \left(1 - \exp \left[-\frac{\Gamma t}{2} \right] \right)^{\frac{L-1}{2} - m}. \quad (15)$$

In Eq. (14), we used the notation $\hat{C}_{\{k_i\}_{i=1}^m} := \prod_{i=1}^m \hat{C}_{-k_i}$ where $\{k_i\}_{i=1}^m$ is an unordered set of indexes (with $k_i > 0$). We see from Eq. (14) that the probabilities P_α of the eigenstates hosting $m-1$ particles with negative energy (and one particle in the \hat{C}_0 mode) are all equal. For those states we can simply set $P_\alpha = P_m$.

So far, we have justified the semiclassical approximation in the large-coupling limit $g_1, g_2 \gg \Gamma$. However, the above description is more general, and allows us to compute the dynamics deep in the topological phase ($g_1 \ll g_2$), when g_1 can become comparable to Γ . In this limit, the energy differences between the eigenstates with the same m appearing in Eq. (14) are of order g_1 , thus the corresponding coherences would not oscillate on a fast timescale. Fortunately, however, the dissipative evolution does not generate such coherences, as can be checked by applying the full master equation, Eq. (8), to a generic eigenstate $|E_\alpha\rangle\langle E_\alpha|$. This is due to a destructive cancellation of amplitudes, which follows from the orthogonality of the eigenmodes. In particular, $\sum_{i=1}^{(L-1)/2} B_{ki} B_{k'i} = 0$ when $k \neq k'$. The semiclassical approximation is still not exact, as the full dynamics generates some coherence between eigenstates with large energy differences, of order g_2 . Thus, it is still necessary to satisfy the condition $g_2 \gg \Gamma$.

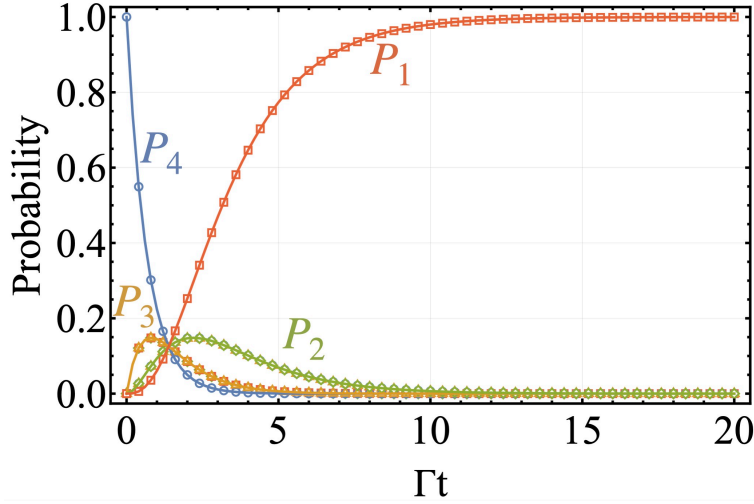


Figure 2. Probability P_m for the system to be found in any many-body eigenstate with m particles as a function of time. The empty markers are obtained by solving the quantum master equation whereas the solid lines are from the semiclassical description. We used $L = 7$ and $g_1/g_2 = \Gamma/g_2 = 0.1$.

To demonstrate the accuracy of the semiclassical approximation when $g_1 \approx \Gamma$, we compare in Fig. 2 two results for the probability $P_m(t)$: One from the numerical solution of the full quantum master equation (8) and another from the semiclassical approximation (15). Clearly we observe an excellent agreement, justifying the semiclassical approach. In passing, we note that the maximum probability appears earlier for states with more particles, which is intuitively appealing.

The semiclassical state in Eq. (14) provides a complete description of the dynamics. For fermionic systems, the state satisfies Wick's theorem [46], hence one can further rewrite it into a Gaussian form [47]:

$$\hat{\rho} = (\det G) \exp \left[\sum_{i,j=0}^{L-1} K_{ij}(t) \hat{f}_i^\dagger \hat{f}_j \right], \quad (16)$$

with the Gaussian kernel K given by:

$$K = \ln [(1 - G)G^{-1}]. \quad (17)$$

Here, G denotes the matrix of single-particle Green's functions, $G_{ij}(t) := \langle \hat{f}_i \hat{f}_j^\dagger \rangle = \text{Tr}[\hat{\rho}(t) \hat{f}_i \hat{f}_j^\dagger]$, which can be conveniently obtained by first evaluating the Green's functions of the normal modes \hat{C}_k . Since the density matrix $\hat{\rho}$ in Eq. (14) is diagonal in the normal modes, we immediately find that $\chi_{kk'} := \langle \hat{C}_k \hat{C}_{k'}^\dagger \rangle = \chi_k \delta_{kk'}$. Explicitly, χ_k is obtained as follows:

$$\chi_k(t) = \begin{cases} 1 - \exp(-\Gamma t/2) & \text{for } k < 0, \\ 0 & \text{for } k = 0, \\ 1 & \text{for } k > 0. \end{cases} \quad (18)$$

Finally, G is related to χ by the same canonical transformation between \hat{f}_i and \hat{C}_k , given in Eqs. (5) and (7). By using Eq. (18), it can be written as

$$G_{ij}(t) = \sum_{k=1}^{(L-1)/2} [(1 - e^{-\Gamma t/2})U_{-k,i}U_{-k,j} + U_{k,i}U_{k,j}], \quad (19)$$

where $U_{\pm k,2i} = A_{ki}$ and $U_{\pm k,2i-1} = \pm B_{ki}$.

The Gaussian form (16) of the density matrix turns out to be extremely powerful when later calculating the entanglement content. We emphasize that for bosons the mixed state in Eq. (14) is not Gaussian anymore, despite having exactly the same form.

3.2. Entanglement measures

Quantifying quantum entanglement [48] is vital in quantum information theory, yet is highly non-trivial. Common entanglement measures include entanglement entropy [49], concurrence [50], and logarithmic negativity (or the closely related negativity) [51, 52]. However, entanglement entropy is applicable only to pure states, while concurrence is practical only for two-qubit systems, whether in pure or mixed states. For mixed states of more general systems, the logarithmic negativity (or negativity) has been widely used as one of very few practically computable entanglement measures. Nevertheless, as it requires finding the eigenvalues of the density matrix after partial transposition, its computational cost increases quickly with system size. To avoid complications arising from partial transposition, quantum mutual information is often used as well. Although mutual information is not an entanglement measure in the strict mathematical sense, it still captures many important aspects of quantum correlations, as well as classical correlations. Below, we will investigate the entanglement content of the mixed state (14) using the logarithmic negativity. However, as we illustrate in Appendix A, the universal features we find are observed in the mutual information as well.

The logarithmic negativity between two subsystems A and B is defined as [51]

$$\mathcal{E}(A, B) := \log_2 \|\hat{\rho}^{TA}\| = \log_2 \|\hat{\rho}^{TB}\|, \quad (20)$$

where $\hat{\rho}^{TA}(\hat{\rho}^{TB})$ is the partial transpose of the density matrix $\hat{\rho}$ with respect to subsystem A (B), and $\|\cdot\|$ denotes the trace norm. As mentioned above and seen in the definition (20), the main obstacle in computing the logarithmic negativity for large systems comes from the partial transposition: If not for the partial transposition, in many cases the trace norm may be calculated without much difficulty, by using the symmetries of the system to decompose the large density matrix into smaller blocks. More specifically, in our model the total number of particles is conserved, i.e., $[\hat{n}_A + \hat{n}_B, \hat{\rho}] = 0$. On the other hand, the partial transpose, $\hat{\rho}^{TA}$ or $\hat{\rho}^{TB}$, violates this symmetry, and one has to deal with the Hilbert space as a whole. Actually, in our model the difference $\hat{n}_A - \hat{n}_B$ in the number of particles is conserved [53], i.e., $[\hat{n}_A - \hat{n}_B, \hat{\rho}^{TA}] = 0$, but the invariant blocks under this symmetry are still exponentially large.

Recently, a new type of logarithmic negativity based on a partial time-reversal transformation has been suggested for fermionic systems [54–56]. Compared to the conventional (or bosonic) logarithmic negativity, this fermionic logarithmic negativity was shown to better capture the contributions to entanglement from Majorana fermions. However, the key advantage from our point of view lies in the fact that the partial time-reversal transformation of a fermionic Gaussian state remains Gaussian, allowing the fermionic logarithmic negativity to be calculated using a $2L \times 2L$ matrix of generalized Green’s functions [54]; that is, with a polynomial amount of resources and time. In our case, as the pairing correlations are zero, the fermionic logarithmic negativity is obtained directly from the $L \times L$ matrix of Green’s functions, see Eq. (19), and we could study half-SSH chains up to $L \sim 10^3$ without difficulties. For the bosonic case, the calculations are limited to relatively short chains.

3.3. Fermionic vs bosonic SSH models

Above, we have already made several remarks on technical differences between the bosonic and fermionic SSH models. Here, we summarize both fundamental and technical differences between them. It is remarkable that, despite these differences, the fermionic and bosonic models share the same universal dynamics of entanglement.

Both bosonic and fermionic systems in the half-SSH model exhibit a chiral symmetry, characterized by the existence of a unitary operator that anti-commutes with the Hamiltonian. This symmetry leads to a degenerate zero-energy subspace and a symmetric single-particle energy spectrum around zero energy. Additionally, the edge mode at zero energy reflects the non-trivial topological character of the band structure.

For large bosonic systems, the size of the Hilbert space poses significant computational challenges. Certain techniques, such as block diagonalization of $\hat{\rho}^{TA}$, are employed to alleviate the computational burden. In contrast, fermionic systems can benefit from the fact that the relevant state is Gaussian, since the partial time-reversal transformation of Eq. (16) remains Gaussian.

In the next Section, we will present our results for both bosonic and fermionic systems in parallel, to highlight the common universal behavior despite the differences summarized above. We attribute the common features of entanglement dynamics to the chiral symmetry and topological properties, especially the zero-energy edge states.

4. Results

We now present our findings, which reveal intriguing dynamical phenomena and provide deeper insights into the relationship between dynamics and topological properties. These results contribute to a better understanding of how topological effects influence dynamical processes, and have significant implications for future developments of quantum technologies.

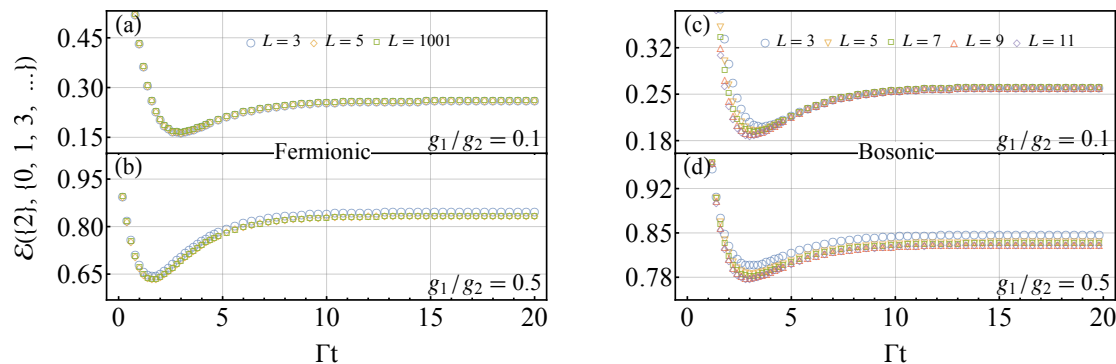


Figure 3. Universal entanglement revival, obtained by computing the logarithmic negativity $\mathcal{E}(\{2\}, \{0, 1, 3, \dots\})$ between the single-site subsystem $\{f_2\}$ and the rest of the chain. Panels (a) and (b) consider the fermionic model at $g_1/g_2 = 0.1$ and 0.5 , respectively. Panels (c) and (d) are for the bosonic model, also using $g_1/g_2 = 0.1$ and 0.5 . Other parameters are $g_2 = 1$ (arbitrary units) and $\Gamma/g_2 = 0.1$.

4.1. Universal entanglement revival

Figure 3 summarizes our main results, concerning the evolution of entanglement between the second even site and the rest of the system. The two left panels of Fig. 3 refer to the fermionic half-SSH chain, where we computed the fermionic logarithmic negativity for two values of g_1 deep in the topologically non-trivial phase ($g_1 \ll g_2$). The two right panels of Fig. 3 show the conventional logarithmic negativity of the bosonic model, using the same set of parameters. In the fermionic case, we could calculate the fermionic logarithmic negativity for systems as large as $L \sim 10^3$, and three representative sizes are shown in panels (a) and (b) of Fig. 3. In the bosonic case, the calculations were limited to relatively small values of L , because of the computational difficulties discussed in Section 3, and panels (c) and (d) show the results for $L = 3, 5, \dots, 11$. In both cases, two distinctive features are clearly seen: First, the entanglement revives after an initial decrease. Considering the very fragile nature of quantum entanglement in the presence of decoherence, an entanglement revival is unusual and has attracted much interest [1–16]. Second, the temporal profile of the entanglement has a universal dependence, i.e., it is almost unaffected by the system size. Although in Fig. 3 we only show the entanglement between site \hat{f}_2 and the remaining sites, $\{\hat{f}_0, \hat{f}_1, \hat{f}_3, \dots, \hat{f}_L\}$, the presence of an universal revival behavior can be observed regardless of the specific choice of partitioning, as long as one subsystem is confined to the left edge. However, the visibility of the revival depends on the partitioning.

As demonstrated in a recent work [16], the entanglement revival behavior is due to a self-purification process directly related to the chiral symmetry and the associated zero-energy mode (not necessarily localized to edges): The system starts from a pure state with relatively large entanglement and, as it undergoes the decoherence process, decays to various intermediate states. Consequently, the purity of the state decreases significantly, which naturally leads to a considerable reduction in entanglement. After

this intermediate stage, however, the system begins to recover its purity (and hence entanglement), because all particles have the fate of decaying out, except for the ones occupying the zero-energy edge mode. Eventually, the system stabilizes to the final state, i.e., the zero-energy mode, which is immune to the decay process. The entanglement in the steady state is always determined by this zero-energy mode.

While the above arguments explains the presence of the revival, its universal character is more intriguing, and is the main topic of the rest of the paper. In the following, we perform a detailed analysis of the size dependence, revealing that the universal behavior can be attributed to the topological feature of the system, especially the zero-energy edge mode.

4.2. Topological effects through the edge state

In Fig. 3, we have seen that the entanglement revival in the deep topological phase ($g_1/g_2 \ll 1$) is universal, having a dynamical profile independent of system size. However, as the ratio g_1/g_2 increases to unity (i.e., the phase boundary of the topological phase is approached), the evolution of entanglement shows significant variations at small system sizes. When $g_1/g_2 = 0.9$, for example, the dynamical profile for $L = 3$ is distinct from the profiles of larger systems ($L = 19, 1001$), as shown in the inset of Fig. 4. We find that the dynamical profiles remain universal as long as the system size is sufficiently large compared to a certain length scale, directly related to the localization length of the zero-energy edge mode. In the following, we examine this crossover scale in detail.

We define two length scales concerning the entanglement revival dynamics: The *crossover length* L_c is defined as the minimum system size which, at a given ratio g_1/g_2 , achieves a universal time dependence. In other words, the dynamical profiles of systems larger than L_c are all universal (within a certain numerical tolerance ϵ). More specifically, let $\mathcal{E}_L(t)$ be the logarithmic negativity for a system of length L . Then, choosing a sufficiently large T , at which the entanglement has reached its asymptotic value, we require that for all $L \geq L_c$

$$\int_0^T dt |\mathcal{E}_L(t) - \mathcal{E}_\infty(t)| \leq \epsilon \int_0^T dt \mathcal{E}_\infty(t). \quad (21)$$

Numerically, we approximate the $L \rightarrow \infty$ limit by taking $L = 1001$. We also choose $T = 20$ and $\epsilon = 0.05$. Figure 4 plots the crossover length L_c (blue empty circles) as a function of g_1/g_2 . It is important to note that L_c closely resembles the localization length ξ of the edge mode (black solid line). For instance, when $g_1/g_2 = 0.9$, the crossover length matches the localization length $L_c \approx \xi \approx 19$. This value is highlighted by a horizontal dashed line in the main panel of Fig. 4. In the inset, we can see that the detailed entanglement profile with $L = 19$ follows quite faithfully the universal dynamics at $L = 1001$.

The second length scale we investigate is the *effective length* L_{eff} of the system. To define L_{eff} , we consider the reduced density matrix $\hat{\rho}_j(t) := \text{Tr}_{i=j+1}^L \hat{\rho}(t)$, obtained by tracing out sites $j + 1, \dots, L$. In general, the reduced density matrix $\hat{\rho}_j(t)$ represents

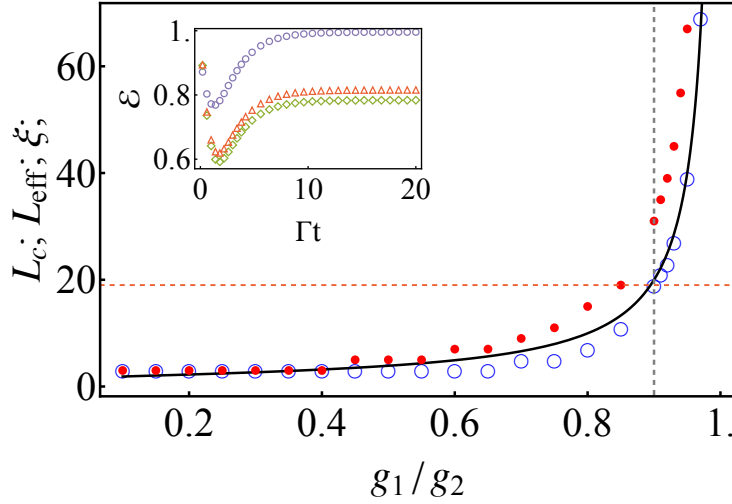


Figure 4. Comparison of the crossover length L_c (blue empty circles) and the effective length L_{eff} (red filled circles) with the localization length ξ of the edge state (black solid line), as a function of the coupling ratio g_1/g_2 . The red dashed line marks the values $L_c \approx 19$, computed at $g_1/g_2 = 0.9$. Inset: time dependence of the logarithmic negativity between the single-site subsystem $\{f_2\}$ and the rest of the chain. Here we take $g_1/g_2 = 0.9$ and $L = 3, 19, 1001$ (from top to bottom).

a physically different state from the full density matrix $\hat{\rho}(t)$. However, in our case, it turns out that $\hat{\rho}_j(t)$ gives physically equivalent results to $\hat{\rho}(t)$, as long as j is larger than a certain length scale, which we refer to as the effective length. That is, the effective length L_{eff} is the minimum length at which the reduced density matrix has the same properties of the full density matrix, $\hat{\rho}_j(t) \approx \hat{\rho}(t)$ for $j \geq L_{\text{eff}}$. The comparison between $\hat{\rho}_j(t)$ and $\hat{\rho}(t)$ is done in terms of the logarithmic negativity, in a manner analogous to Eq. (21). More precisely, in Eq. (21) we substitute $\mathcal{E}_L(t) \rightarrow \mathcal{E}_j(t)$, where $\mathcal{E}_j(t)$ is the logarithmic negativity obtained from $\hat{\rho}_j(t)$. Ideally, we would compute $\hat{\rho}_j(t)$ from the full density matrix $\hat{\rho}(t)$ of the infinite half-SSH chain, i.e., in the limit $L \rightarrow \infty$. In practice, we can choose a sufficiently large value of L and, as before, we have used $L = 1001$ in our numerical calculations.

The explicit dependence of L_{eff} on g_1/g_2 is shown in Fig. 4. As seen, also the effective length L_{eff} (red filled circles) agrees well with the localization length ξ of the edge mode. That both L_c and L_{eff} follow closely the localization length ξ strongly suggest that the spatial range of the edge mode is a critical factor in determining the onset of the universal entanglement revival behavior.

Another feature that supports the topological origin of the entanglement revival is the visibility, defined as the difference between the asymptotic value ($t \rightarrow \infty$) and the minimum of the logarithmic negativity. The details of the visibility differ between the fermionic and bosonic cases, and they are also affected by system parameters. However, as illustrated in Fig. 5 for a long fermionic chain, we find the following generic qualitative features: The visibility is zero at $g_1/g_2 = 0$ and first increases with g_1/g_2 , reaching a maximum around $g_1/g_2 \approx 0.5$. Then, it sharply drops to zero (i.e., the entanglement

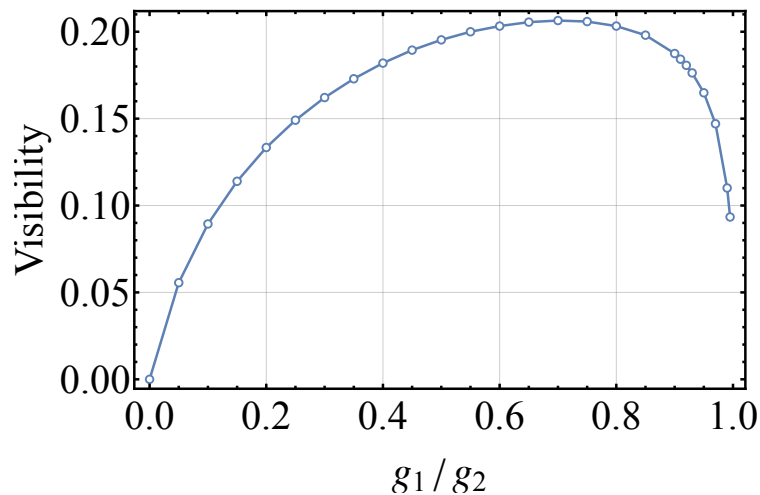


Figure 5. The visibility of entanglement revival as a function of the coupling ratio g_1/g_2 , for $L = 1001$ and $\Gamma/g_2 = 0.1$.

revival disappears) as g_1/g_2 approaches 1. The visibility vanishing at $g_1/g_2 = 0$ is trivial, since the unit cells are decoupled. However, the disappearance of the entanglement revival when $g_1/g_2 \rightarrow 1$, which is the boundary of the topological phase, strongly suggests that the entanglement revival is closely connected with the edge mode.

Finally, while in this section we have exclusively discussed the logarithmic negativity, the universal revival can also be found in the mutual information (see [Appendix A](#)). The von Neumann and Rényi entropy densities exhibit a size-independent behavior as well (see [Appendix B](#)), suggesting that the topological properties of the system influence more generally the dynamical evolution and robustness of local correlations, both quantum and classical.

5. Conclusion

In this study of the fermionic and bosonic SSH models, characterized by the presence of a chiral symmetry, we explored the dynamics of entanglement of a single site with the rest of the chain, in the presence of decoherence which preserves the chiral symmetry. Our results reveal a remarkable entanglement revival which, for a fixed coupling ratio, acquires a universal profile when the system length exceeds the localization length of the edge states. Therefore, the effective length scale for the onset of universality can be identified with the localization length. These findings highlight a direct connection between the universal entanglement revival and the topological phase.

Acknowledgments

C.D. and M.-S.C. have been supported by the National Research Function (NRF) of Korea (Grant Nos. 2022M3H3A106307411 and 2023R1A2C1005588) and by the

Ministry of Education through the BK21 Four program. S.C. acknowledges support from the Innovation Program for Quantum Science and Technology (Grant No. 2021ZD0301602) and the National Science Association Funds (Grant No. U2230402).

Appendix A. Mutual information

The mutual information is a measure of total correlations, both classical and quantum, between two subsystems. It provides a different perspective on the state of the system than entanglement measures, like the logarithmic negativity. Furthermore, the mutual information is usually easier to compute than most entanglement measures, making it a practical alternative for larger systems. Here, we show that the mutual information, like the logarithmic negativity, exhibits a universal entanglement revival, which indicates that universality is not limited to a specific entanglement measure.

The mutual information between subsystems A and B is defined as:

$$I_\gamma(A, B) := S_\gamma(\hat{\rho}_A) + S_\gamma(\hat{\rho}_B) - S_\gamma(\hat{\rho}), \quad (\text{A.1})$$

where $\hat{\rho}_{A/B}$ is the reduced density matrix of subsystem A/B and $\hat{\rho}$ the full density matrix, while the Rényi entropy of order γ is defined as:

$$S_\gamma(\hat{\rho}) := \frac{1}{1-\gamma} \log_2 \text{Tr}(\hat{\rho}^\gamma). \quad (\text{A.2})$$

In the limit $\gamma \rightarrow 1$, the Rényi entropy becomes the von Neumann entropy, $S_{\text{vN}}(\hat{\rho}) = -\text{Tr}(\hat{\rho} \log_2 \hat{\rho})$. However, computing the von Neumann entropy can still be computationally intensive for large systems. In the case with $\gamma = 2$, the Rényi entropy simplifies to the second-order Rényi entropy, $S_2(\hat{\rho}) = -\log_2 \text{Tr}(\hat{\rho}^2)$, which is easier to compute and advantageous for large or complex systems.

For fermionic Gaussian states, the von Neumann entropy can be calculated efficiently from the correlation function [57]. In Fig. A1, we can observe that the entanglement revival might disappear in certain limits, such as $g_1 \ll g_2$, because the mutual information is not a proper measure of quantum entanglement. However, the universal behavior always persists, which is in agreement with the results for the logarithmic negativity presented in the main text. In addition, both measures suggest that, for a fixed coupling ratio g_1/g_2 , the universal behavior can be observed when the size of the half-SSH model exceeds a certain crossover length. The consistency in behavior between the two measures underscores the robustness of the universal entanglement revival phenomenon, confirming once more that the universal behavior is determined by the inherent properties of the system.

For the bosonic case, computing the von Neumann mutual information is more challenging than fermions, since the Hilbert space still grows exponentially with the chain length, increasing the difficulty in computing eigenvalues. Currently, we are able to calculate the von Neumann mutual information up to $L = 13$. Figure A2 illustrates the entanglement dynamics for bosonic systems with different coupling ratios and chain

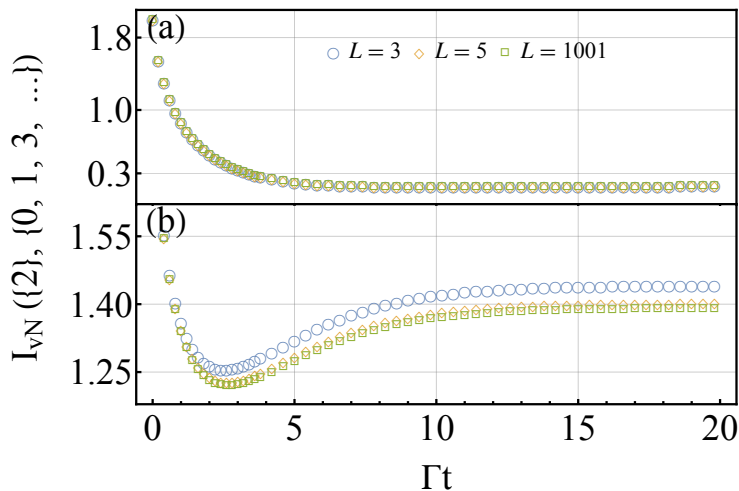


Figure A1. Time dependence of the von Neumann mutual information in the fermionic model. $I_{\text{vN}}(\{2\}, \{0, 1, 3, \dots\})$ indicates the von Neumann mutual information between the single-site subsystem $\{\hat{f}_2\}$ and the rest of the chain. In panels (a) and (b) we use $g_1/g_2 = 0.1$ and 0.5 , respectively. In both panels, $\Gamma/g_2 = 0.1$.

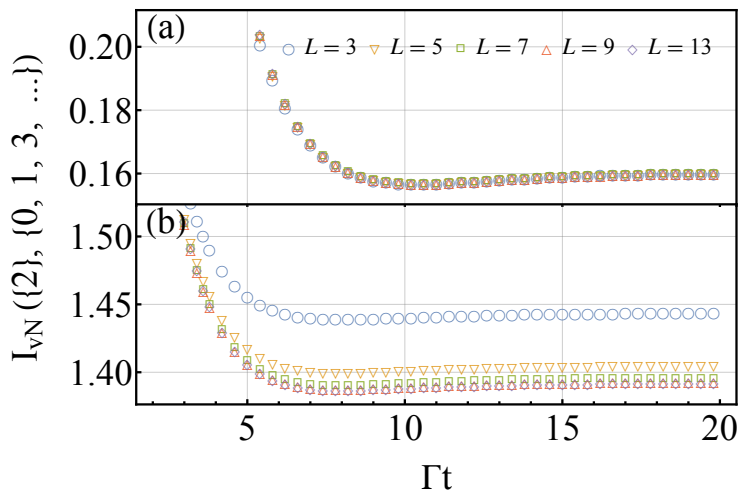


Figure A2. The revival behavior of von Neumann mutual information in the bosonic model for coupling ratios (a) $g_1/g_2 = 0.1$ and (b) $g_1/g_2 = 0.5$. Here, we set $\Gamma/g_2 = 0.1$.

lengths. As seen, despite the maximum length being much shorter than for fermions, the universal behavior is still present. Thus, the conclusions for bosons are very similar to those for fermions in Fig. A1, and to the behavior of the logarithmic negativity.

Due to the limitations in calculating the von Neumann mutual information for bosonic systems, we extended our analysis to the Rényi mutual information, which can be obtained for larger system sizes (specifically, we consider $L = 11, 15, 19$, and 23). As shown in Fig. A3, also the Rényi mutual information displays a universal revival. The larger accessible system sizes allow us to obtain good convergence also in Fig. A3(b), where a larger coupling ratio $g_1/g_2 = 0.5$ is assumed. This extension further confirms

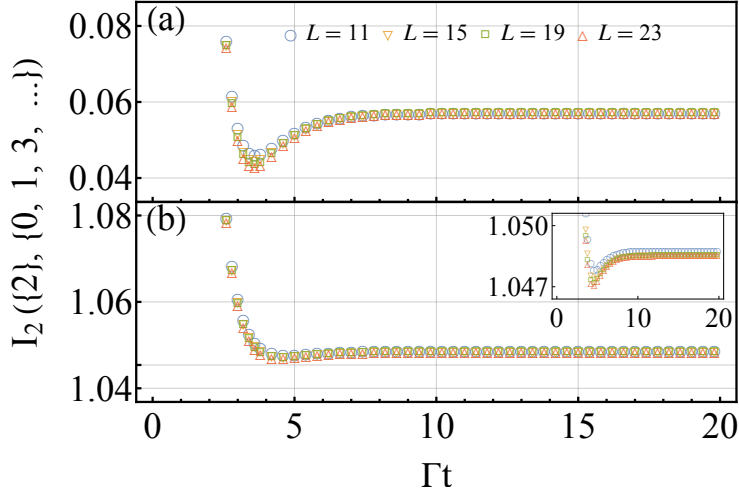


Figure A3. Revival behavior of the Rényi mutual information in the bosonic model, for coupling ratios (a) $g_1/g_2 = 0.1$ and (b) $g_1/g_2 = 0.5$. We denote the Rényi mutual information between the single-site subsystem $\{f_2\}$ and the rest of the chain by $I_2(\{2\}, \{0, 1, 3, \dots\})$. The inset of panel (b) is a zoom-in of the main plot. We have used $\Gamma/g_2 = 0.1$.

that the universal behavior is not restricted to the von Neumann mutual information and logarithmic negativity, offering new evidence of its robustness in larger bosonic systems.

Appendix B. Entropy density

We also consider the average entropy $s_\gamma(\hat{\rho}) = S_\gamma(\hat{\rho})/n$, where $S_\gamma(\hat{\rho})$ is defined in Eq. (A.2) and $n = (L - 1)/2$ is the number of two-site unit cells. These quantities can be easily evaluated within the semiclassical approximation of $\hat{\rho}$, given by Eqs. (14) and (15). In particular, the von Neumann entropy density $s_{\text{vN}}(\rho)$ is obtained as follows:

$$s_{\text{vN}} = -\log_2(1 - e^{-\Gamma t/2}) + e^{-\Gamma t/2} \log_2(-1 + e^{\Gamma t/2}), \quad (\text{B.1})$$

and the Rényi entropy density of order 2 reads:

$$s_2 = -\log_2(1 + 2e^{-\Gamma t} - 2e^{-\Gamma t/2}). \quad (\text{B.2})$$

The qualitative time dependence of these quantities differs from the logarithmic negativity, since the system is in a pure state at $t = 0$ and $t \rightarrow \infty$ (when the entropy is zero) and there is no revival behavior. Instead, the entropy density attains its maximum value $s_{\text{vN}} = s_2 = 1$ at $\Gamma t = 2 \ln 2$. The increase of the entropy at intermediate times is in qualitative agreement with the reduction of purity and the occurrence of a minimum in the logarithmic negativity. However, in contrast to the entanglement, the maximum entropy always occurs at $\Gamma t = 2 \ln 2$, independent of the coupling strengths $g_{1,2}$. This difference is due to the fact that the probabilities of the eigenstates, given in

Eq. (15), do not depend on $g_{1,2}$. Instead, the entanglement is obviously affected by the specific eigenstates which diagonalize $\hat{\rho}$, thus the position of the minimum depends the coupling ratio g_1/g_2 . Despite these remarks, we note that both Eqs. (B.1) and (B.2) are independent on L , i.e., they display a universal behavior, demonstrating that local quantum correlations are robust with respect to the overall system size. These results suggest that the robustness of local quantum correlations is likely due to the topological properties of the SSH model, contributing to the stability of the entanglement revival under different conditions.

References

- [1] Życzkowski K, Horodecki P, Horodecki M and Horodecki R 2001 Dynamics of quantum entanglement *Phys. Rev. A* **65**(1) 012101
- [2] Aolita L, de Melo F and Davidovich L 2015 Open-system dynamics of entanglement: a key issues review *Reports on Progress in Physics* **78** 042001
- [3] Tanaś R and Ficek Z 2004 Entangling two atoms via spontaneous emission *Journal of Optics B: Quantum and Semiclassical Optics* **6** S90
- [4] Benatti F and Floreanini R 2006 Entangling oscillators through environment noise *Journal of Physics A: Mathematical and General* **39** 2689
- [5] Cunha M O T 2007 The geometry of entanglement sudden death *New Journal of Physics* **9** 237
- [6] Abdel-Aty M and Yu T 2008 Entanglement sudden birth of two trapped ions interacting with a time-dependent laser field *Journal of Physics B: Atomic, Molecular and Optical Physics* **41** 235503
- [7] Ficek Z and Tanaś R 2006 Dark periods and revivals of entanglement in a two-qubit system *Phys. Rev. A* **74**(2) 024304
- [8] Ficek Z and Tanaś R 2008 Delayed sudden birth of entanglement *Phys. Rev. A* **77**(5) 054301
- [9] Paz J P and Roncaglia A J 2008 Dynamics of the entanglement between two oscillators in the same environment *Phys. Rev. Lett.* **100**(22) 220401
- [10] Drumond R C and Cunha M O T 2009 Asymptotic entanglement dynamics and geometry of quantum states *Journal of Physics A: Mathematical and Theoretical* **42** 285308
- [11] Das S and Agarwal G S 2009 Decoherence effects in interacting qubits under the influence of various environments *Journal of Physics B: Atomic, Molecular and Optical Physics* **42** 205502
- [12] Orszag M and Hernandez M 2010 Coherence and entanglement in a two-qubit system *Adv. Opt. Photon.* **2** 229–286
- [13] Amico M, Berman O L and Kezerashvili R Y 2018 Dissipative quantum entanglement dynamics of two and three qubits due to the dynamical lamb effect *Phys. Rev. A* **98**(4) 042325
- [14] Lakhfif A, Hidki A, El Qars J and Nassik M 2022 Pairwise entanglement in a three-cavity optomechanical system *Physics Letters A* **445** 128247 ISSN 0375-9601
- [15] Nunavath N, Mishra S and Pathak A 2023 Open quantum system dynamics of x-states: Entanglement sudden death and sudden birth *Modern Physics Letters A* **38** 2350056 (Preprint arXiv:<https://doi.org/10.1142/S0217732323500566>)
- [16] Chen D, Chesi S and Choi M S 2024 Self-purification and entanglement revival in lambda matter *New Journal of Physics* **26** 013018 URL <https://dx.doi.org/10.1088/1367-2630/ad18ec>
- [17] Su W P, Schrieffer J R and Heeger A J 1979 Solitons in polyacetylene *Phys. Rev. Lett.* **42**(25) 1698–1701 URL <https://link.aps.org/doi/10.1103/PhysRevLett.42.1698>
- [18] Asbóth J K, Oroszlány L and Pályi A 2016 *A Short Course on Topological Insulators (Lecture Notes in Physics vol 919)* (Springer, Cham)
- [19] Shen S Q 2017 *Topological Insulators: Dirac Equation in Condensed Matter* (Springer Singapore)
- [20] Kitaev A 2003 Fault-tolerant quantum computation by anyons *Annals of Physics*

- 303** 2–30 ISSN 0003-4916 URL <https://www.sciencedirect.com/science/article/pii/S0003491602000180>
- [21] Michael H Freedman, Alexei Kitaev, M J L and Wang Z 2003 Topological quantum computation *Bulletin of the American Mathematical Society* **40** 31–38 URL <https://www.ams.org/journals/bull/2003-40-01/S0273-0979-02-00964-3/>
- [22] Nayak C, Simon S H, Stern A, Freedman M and Das Sarma S 2008 Non-abelian anyons and topological quantum computation *Rev. Mod. Phys.* **80**(3) 1083–1159 URL <https://link.aps.org/doi/10.1103/RevModPhys.80.1083>
- [23] Bomantara R W and Gong J 2018 Quantum computation via floquet topological edge modes *Phys. Rev. B* **98**(16) 165421 URL <https://link.aps.org/doi/10.1103/PhysRevB.98.165421>
- [24] Bomantara R W and Gong J 2018 Simulation of non-abelian braiding in majorana time crystals *Phys. Rev. Lett.* **120**(23) 230405 URL <https://link.aps.org/doi/10.1103/PhysRevLett.120.230405>
- [25] Lahtinen V and Pachos J K 2017 A Short Introduction to Topological Quantum Computation *SciPost Phys.* **3** 021 URL <https://scipost.org/10.21468/SciPostPhys.3.3.021>
- [26] Halperin B I 1982 Quantized hall conductance, current-carrying edge states, and the existence of extended states in a two-dimensional disordered potential *Phys. Rev. B* **25**(4) 2185–2190 URL <https://link.aps.org/doi/10.1103/PhysRevB.25.2185>
- [27] Büttiker M 1988 Absence of backscattering in the quantum hall effect in multiprobe conductors *Phys. Rev. B* **38**(14) 9375–9389 URL <https://link.aps.org/doi/10.1103/PhysRevB.38.9375>
- [28] Niu Q and Thouless D J 1984 Quantised adiabatic charge transport in the presence of substrate disorder and many-body interaction *Journal of Physics A: Mathematical and General* **17** 2453 URL <https://dx.doi.org/10.1088/0305-4470/17/12/016>
- [29] Hasan M Z and Kane C L 2010 Colloquium: Topological insulators *Rev. Mod. Phys.* **82**(4) 3045–3067 URL <https://link.aps.org/doi/10.1103/RevModPhys.82.3045>
- [30] Qi X L and Zhang S C 2011 Topological insulators and superconductors *Rev. Mod. Phys.* **83**(4) 1057–1110 URL <https://link.aps.org/doi/10.1103/RevModPhys.83.1057>
- [31] Ryu S, Schnyder A P, Furusaki A and Ludwig A W W 2010 Topological insulators and superconductors: tenfold way and dimensional hierarchy *New Journal of Physics* **12** 065010
- [32] Kawasaki M, Mochizuki K and Obuse H 2022 Topological phases protected by shifted sublattice symmetry in dissipative quantum systems *Phys. Rev. B* **106**(3) 035408 URL <https://link.aps.org/doi/10.1103/PhysRevB.106.035408>
- [33] Huang Y W, Yang P Y and Zhang W M 2020 Quantum theory of dissipative topological systems *Phys. Rev. B* **102**(16) 165116 URL <https://link.aps.org/doi/10.1103/PhysRevB.102.165116>
- [34] Diehl S, Rico E, Baranov M A and Zoller P 2011 Topology by dissipation in atomic quantum wires *Nature Physics* **7** 971–977 ISSN 1745-2481 URL <https://doi.org/10.1038/nphys2106>
- [35] Bardyn C E, Baranov M A, Kraus C V, Rico E, İmamoğlu A, Zoller P and Diehl S 2013 Topology by dissipation *New Journal of Physics* **15** 085001 URL <https://dx.doi.org/10.1088/1367-2630/15/8/085001>
- [36] Rivas A, Viyuela O and Martin-Delgado M A 2013 Density-matrix chern insulators: Finite-temperature generalization of topological insulators *Phys. Rev. B* **88**(15) 155141 URL <https://link.aps.org/doi/10.1103/PhysRevB.88.155141>
- [37] Viyuela O, Rivas A and Martin-Delgado M A 2012 Thermal instability of protected end states in a one-dimensional topological insulator *Phys. Rev. B* **86**(15) 155140 URL <https://link.aps.org/doi/10.1103/PhysRevB.86.155140>
- [38] Dangel F, Wagner M, Cartarius H, Main J and Wunner G 2018 Topological invariants in dissipative extensions of the su-schrieffer-heeger model *Phys. Rev. A* **98**(1) 013628 URL <https://link.aps.org/doi/10.1103/PhysRevA.98.013628>
- [39] Madsen L S, Laudenbach F, Askarani M F, Rortais F, Vincent T, Bulmer J F F, Miatto

- F M, Neuhaus L, Helt L G, Collins M J, Lita A E, Gerrits T, Nam S W, Vaidya V D, Menotti M, Dhand I, Vernon Z, Quesada N and Lavoie J 2022 Quantum computational advantage with a programmable photonic processor *Nature* **606** 75–81 ISSN 1476-4687 URL <https://doi.org/10.1038/s41586-022-04725-x>
- [40] O'Brien J L, Furusawa A and Vucčković J 2009 Photonic quantum technologies *Nature Photonics* **3** 687–695 ISSN 1749-4893 URL <https://doi.org/10.1038/nphoton.2009.229>
- [41] Yuan G, Chen Y, Lu J, Wu S, Ye Z, Qian L and Chen G 2024 Quantum computing for databases: Overview and challenges (*Preprint* arXiv:2405.12511) URL <https://arxiv.org/abs/2405.12511>
- [42] Lu L, Joannopoulos J D and Soljačić M 2014 Topological photonics *Nature Photonics* **8** 821–829 ISSN 1749-4893 URL <https://doi.org/10.1038/nphoton.2014.248>
- [43] Rechtsman M C, Zeuner J M, Plotnik Y, Lumer Y, Podolsky D, Dreisow F, Nolte S, Segev M and Szameit A 2013 Photonic floquet topological insulators *Nature* **496** 196–200 ISSN 1476-4687 URL <https://doi.org/10.1038/nature12066>
- [44] Prosen T 2008 Third quantization: a general method to solve master equations for quadratic open fermi systems *New Journal of Physics* **10** 043026 URL <https://dx.doi.org/10.1088/1367-2630/10/4/043026>
- [45] Alba V and Carollo F 2023 Logarithmic negativity in out-of-equilibrium open free-fermion chains: An exactly solvable case *SciPost Phys.* **15** 124 URL <https://scipost.org/10.21468/SciPostPhys.15.3.124>
- [46] Mahan G D 2000 *Many-Particle Physics* 3rd ed (Springer)
- [47] Peschel I 2003 Calculation of reduced density matrices from correlation functions *Journal of Physics A: Mathematical and General* **36** L205 URL <https://dx.doi.org/10.1088/0305-4470/36/14/101>
- [48] Plenio M B and Virmani S 2007 An introduction to entanglement measures *Quantum Info. Comput.* **7** 1 ISSN 1533-7146
- [49] Bennett C H, Bernstein H J, Popescu S and Schumacher B 1996 Concentrating partial entanglement by local operations *Phys. Rev. A* **53**(4) 2046–2052 URL <https://link.aps.org/doi/10.1103/PhysRevA.53.2046>
- [50] Wootters W K 1998 Entanglement of formation of an arbitrary state of two qubits *Phys. Rev. Lett.* **80**(10) 2245–2248 URL <https://link.aps.org/doi/10.1103/PhysRevLett.80.2245>
- [51] Plenio M B 2005 Logarithmic negativity: A full entanglement monotone that is not convex *Phys. Rev. Lett.* **95**(9) 090503
- [52] Eisert J and Plenio M B 1999 A comparison of entanglement measures *Journal of Modern Optics* **46** 145–154
- [53] Qiu J, Chen D, Wang Y D and Chesi S 2022 Enhancing photon entanglement in a three-mode optomechanical system via imperfect phonon measurements *Communications in Theoretical Physics* **74** 055105 URL <https://dx.doi.org/10.1088/1572-9494/ac64f4>
- [54] Shapourian H, Shiozaki K and Ryu S 2017 Partial time-reversal transformation and entanglement negativity in fermionic systems *Phys. Rev. B* **95**(16) 165101 URL <https://link.aps.org/doi/10.1103/PhysRevB.95.165101>
- [55] Shapourian H and Ryu S 2019 Finite-temperature entanglement negativity of free fermions *Journal of Statistical Mechanics: Theory and Experiment* **2019** 043106 URL <https://dx.doi.org/10.1088/1742-5468/ab11e0>
- [56] Shapourian H and Ryu S 2019 Entanglement negativity of fermions: Monotonicity, separability criterion, and classification of few-mode states *Phys. Rev. A* **99**(2) 022310 URL <https://link.aps.org/doi/10.1103/PhysRevA.99.022310>
- [57] Casini H and Huerta M 2009 Entanglement entropy in free quantum field theory *Journal of Physics A: Mathematical and Theoretical* **42** 504007 URL <https://dx.doi.org/10.1088/1751-8113/42/50/504007>